Received: 30 June 2023 | Accepted: 26 October 2023

DOI: 10.1002/pamm.202300123

RESEARCH ARTICLE

Nonlinear cable computations using high-order solid elements with *hp*-adaptive refinement for anisotropic plasticity

André Hildebrandt-Raj[1] | **Prateek Sharma**[2] | **Stefan Diebels**[2] | **Alexander Düster**[1]

[1]Numerical Structural Analysis with Application in Ship Technology (M-10), Hamburg University of Technology, Hamburg, Germany

[2]Applied Mechanics, Saarland University, Saarbrücken, Germany

Correspondence
André Hildebrandt-Raj, Numerical Structural Analysis with Application in Ship Technology (M-10), Hamburg University of Technology, Am Schwarzenberg-Campus 4 C, D-21073 Hamburg, Germany.
Email: andre.hildebrandt@tuhh.de

Funding information
The support of the DFG (German Research Foundation) under grant number DU 405/14-2 and DI 430/43-2 is gratefully acknowledged.

Abstract

Cables are slender structural elements, that are found in many engineering structures and are exposed to large displacements while experiencing small or large local strains during their installation or in dynamic environments. To address the complexity of their inner structure, an effective material model with anisotropic properties in the elastic and elastoplastic domain is utilized, allowing for a simplified representation that overcomes numerical challenges associated with a fully resolved model. This article focuses on enhancing the representation of local discontinuities arising from the plastic front using *hp*-refinement. The described workflow is applied to a perforated plate benchmark example and a cable subjected to torsion. Results indicate that the *hp*-refinement achieves a fast convergence and on average uses fewer degrees of freedom to achieve similar accuracy as compared to pure *h*-refinement or pure *p*-refinement.

1 | INTRODUCTION

Cables are slender structural elements, that are commonly found in engineering structures. They serve multiple purposes, such as being used as components in bridges, ski lifts, and tensile structures, as well as functioning as electrical conductors or signal transmitters. As a result, there is a wide range of layouts and use cases, ranging from small cables serving as simple copper wires to large compositions like undersea cables that enable the creation of the World Wide Web or offshore power lines transmitting renewable energy.

Typically, the cross-section of a cable contains various materials, including rubber for insulation and protective jackets, conductive metals like copper, and sometimes woven fibers to provide electrical shielding or enhance structural durability. Dealing with the different materials and accounting for interactions between the inner parts, which occur through frictional contact, poses numerical challenges and requires significant computational resources. To reduce computational costs, a simplified approach is pursued, that represents the cable as a single material model incorporating anisotropic

TABLE 1 Hyperelastic material parameters.

$\alpha_1 = -\alpha_4 - \alpha_7 - \alpha_8 - 2\alpha_{10}$	$\alpha_5 = \frac{1}{4}(\frac{1-\nu_{13}\nu_{31}}{m}E_2 - 8\alpha_{11})$	$\alpha_9 = E_3\frac{\nu_{23}+\nu_{13}\nu_{21}}{4m}$
$\alpha_2 = -\alpha_5 - \alpha_7 - \alpha_9 - 2\alpha_{11}$	$\alpha_6 = \frac{1}{4}(\frac{1-\nu_{12}\nu_{21}}{m}E_3 - 8\alpha_{12})$	$\alpha_{10} = \frac{1}{4}(G_{12} + G_{13} - G_{23})$
$\alpha_3 = -\alpha_6 - \alpha_8 - \alpha_9 - 2\alpha_{12}$	$\alpha_7 = E_2\frac{\nu_{12}+\nu_{13}\nu_{32}}{4m}$	$\alpha_{11} = \frac{1}{4}(G_{12} - G_{13} + G_{23})$
$\alpha_4 = \frac{1}{4}(\frac{1-\nu_{23}\nu_{32}}{m}E_1 - 8\alpha_{10})$	$\alpha_8 = E_3\frac{\nu_{13}+\nu_{12}\nu_{23}}{4m}$	$\alpha_{12} = \frac{1}{4}(-G_{12} + G_{13} + G_{23})$

properties in the hyperelastic and elastoplastic regimes [1], without explicitly considering the geometric details of the inner structure.

This framework focuses on the simulation of cables that experience large displacements coupled with either small or large local strains. Large local strains can arise through contact with other objects, for instance, during the installation of a cable when it is pulled over edges or when a robotic arm operates. To accurately capture the curved geometry while maintaining computational efficiency, anisotropic solid elements with high-order hierarchic shape functions [2] are employed within the nonlinear finite element framework. By utilizing quasi-regional mapping techniques, the curved geometry can be effectively represented using only a small number of elements. However, when incorporating anisotropic behavior, careful attention must be given to the mapping function to prevent the introduction of artificial strains [3]. This work focuses on improving the simulation of local phenomena like plasticity or contact using *hp*-refinement [4]. To this end the general workflow and the necessary steps are described, which then result in a study of a perforated plate benchmark example and a brief demonstration simulation of a torsion test of a cable in three dimensions.

2 | THEORY

Considering the occurrence of large local strains during loading, it becomes necessary to account for nonlinearities in the finite element method (FEM). These nonlinearities encompass geometric aspects due to large displacements and material nonlinearities due to large strains. Therefore, we propose an anisotropic material model [1, 5] based on a strain energy density function. According to ref. [5], we utilize the orthotropic material model that relies on three directions $\boldsymbol{v}_i$ in the reference configuration, which define structural tensors $\boldsymbol{M}_i = \boldsymbol{v}_i \otimes \boldsymbol{v}_i$ for $i = 1, 2, 3$, where $\otimes$ denotes the dyadic product. These structural tensors, in conjunction with the elastic right Cauchy-Green tensor $\boldsymbol{C}_\mathrm{e} = \boldsymbol{F}_\mathrm{e}^\mathrm{T}\boldsymbol{F}_\mathrm{e}$, are used to compute the invariants

$$J_i = \mathrm{tr}[\boldsymbol{M}_i\boldsymbol{C}_\mathrm{e}], \quad \text{for } i = 1, 2, 3, \tag{1}$$

$$J_{i+3} = \mathrm{tr}[\boldsymbol{M}_i\boldsymbol{C}_\mathrm{e}^2], \quad \text{for } i = 1, 2, 3. \tag{2}$$

The strain energy density function can then be defined as

$$\Psi_\mathrm{e} = \sum_{i=1}^{3}\left[\alpha_i J_i + \frac{\alpha_{i+3}}{2}J_i^2 + \alpha_{i+9}J_{i+3}\right] + \alpha_9 J_1 J_2 + \alpha_8 J_1 J_3 + \alpha_9 J_2 J_3, \tag{3}$$

where α_i for $i = 1, \cdots, 12$ are the material parameters, see Table 1. The material parameters that have to be specified are the Young's moduli E_i, Poisson's ratios ν_{ij}, and shear moduli G_{ij} for all three directions. The auxiliary parameter m is given by $m = 1 - \nu_{12}\nu_{21} - \nu_{23}\nu_{32} - \nu_{13}\nu_{31} - 2\nu_{12}\nu_{23}\nu_{31}$ and the Poisson's ratios are related through the Young's moduli by the relation $\frac{\nu_{ij}}{E_i} = \frac{\nu_{ji}}{E_j}$.

In order to reduce the total number of nine independent material parameters plus three orthogonal directions the assumption of transverse isotropy is incorporated. This assumption can be justified by the approximate isotropy, that the analyzed cable specimens exhibit within the cross section.

This assumption can be incorporated in the given material model by setting the quantities $E_2 = E_3$, $G_{12} = G_{13}$, $G_{23} = \frac{E_2}{2(1+\nu_{23})}$, $\nu_{13} = \nu_{12}$ and leaves five independent material parameters. Further, the relation $\boldsymbol{M}_1 + \boldsymbol{M}_2 + \boldsymbol{M}_3 = \boldsymbol{I}$ can be exploited to reduce the number of directions $\boldsymbol{v}_i$, that have to be defined in the hyperelastic domain.

To this end the strain energy density function in Equation (3) can be reformulated. This is presented here in three steps:

Step 1, based on the reduction to transverse isotropy the equation $\alpha_2 = \alpha_3$ unfolds and $\alpha_1' = \alpha_1 - \alpha_2$ can be introduced. Combining this with the invariants J_i, $i = 1, 2, 3$ it can be rearranged to

$$\begin{aligned}\alpha_1 J_1 + \alpha_2 J_2 + \alpha_3 J_3 &= \mathrm{tr}((\alpha_1 \boldsymbol{M}_1 + \alpha_2 \boldsymbol{M}_2 + \alpha_3 \boldsymbol{M}_3)\boldsymbol{C}_\mathrm{e}),\\ &= \alpha_2 \mathrm{tr}(\boldsymbol{C}_\mathrm{e}) + \alpha_1' J_1.\end{aligned} \tag{4}$$

Step 2, the equation $\alpha_{11} = \alpha_{12}$ can be used and an auxiliary variable $\alpha_{10}' = \alpha_{10} - \alpha_{11}$ is introduced. Combining them with the invariants J_i, $i = 4, 5, 6$, a split into an isotropic and an enhanced part is possible

$$\begin{aligned}\alpha_{10} J_4 + \alpha_{11} J_5 + \alpha_{12} J_6 &= \mathrm{tr}((\alpha_{10} \boldsymbol{M}_1 + \alpha_{11} \boldsymbol{M}_2 + \alpha_{12} \boldsymbol{M}_3)\boldsymbol{C}_\mathrm{e}^2),\\ &= \alpha_{11} \mathrm{tr}(\boldsymbol{C}_\mathrm{e}^2) + \alpha_{10}' J_4.\end{aligned} \tag{5}$$

Step 3 is similar to the above steps, the equations $\alpha_5 = \alpha_6$ and $\alpha_7 = \alpha_8$ are directly given. Taking a closer look at α_5 and α_9 it becomes clear, that they are equal as well ($m = 1 - 2\nu_{12}\nu_{21} - \nu_{23}^2 - 2\nu_{12}\nu_{23}\nu_{21}$):

$$\begin{aligned}\alpha_5 &= \frac{1 - \nu_{13}\nu_{31}}{4m} E_2 - 8\alpha_{11} = \frac{1 - \nu_{12}\nu_{21}}{4m} E_2 - \frac{E_2}{(1 + \nu_{23})} = \frac{1 - \nu_{12}\nu_{21} - 1 + \nu_{23} + 2\nu_{12}\nu_{21}}{4(1 + \nu_{23})(1 - \nu_{23} - 2\nu_{12}\nu_{21})} E_2,\\ &= \frac{\nu_{23} + \nu_{12}\nu_{21}}{4m} E_2 = \alpha_9.\end{aligned} \tag{6}$$

In this way some auxiliary variables $\alpha_7' = \alpha_7 - \alpha_5$ and $\alpha_4' = \alpha_4 - \alpha_5$ can be defined to split the remaining invariants in an isotropic and enhanced part:

$$\begin{aligned}\frac{\alpha_{i+3}}{2} J_i^2 + \alpha_7 J_1 J_2 + \alpha_8 J_1 J_3 + \alpha_9 J_2 J_3 &= \frac{J_1}{2}(\alpha_5(J_1 + J_2 + J_3) + \alpha_7'(J_2 + J_3) + \alpha_4' J_1)\\ &\quad + \frac{J_2}{2}(\alpha_5(J_1 + J_2 + J_3) + \alpha_7' J_1) + \frac{J_3}{2}(\alpha_5(J_1 + J_2 + J_3) + \alpha_7' J_1)\\ &= \frac{\alpha_5}{2}\mathrm{tr}(\boldsymbol{C}_\mathrm{e})^2 + \alpha_7'(\mathrm{tr}(\boldsymbol{C}_\mathrm{e}) - J_1)J_1 + \frac{\alpha_4'}{2} J_1^2\end{aligned} \tag{7}$$

This leads to the modified strain energy density function $W_\mathrm{e} = W_\mathrm{e,iso} + W_\mathrm{e,tr}$

$$W_\mathrm{e,iso} = \alpha_2 \mathrm{tr}(\boldsymbol{C}_\mathrm{e}) + \frac{\alpha_5}{2}\mathrm{tr}(\boldsymbol{C}_\mathrm{e})^2 + \alpha_{11}\mathrm{tr}(\boldsymbol{C}_\mathrm{e}^2) \tag{8}$$

$$W_\mathrm{e,tr} = \alpha_1' J_1 + \alpha_7' \mathrm{tr}(\boldsymbol{C}_\mathrm{e}) J_1 + \left(\frac{\alpha_4'}{2} - \alpha_7'\right) J_1^2 + \alpha_{10}' J_4 \tag{9}$$

If the material parameters for Ψ_e are chosen to be transversely isotropic, the equation $\Psi_\mathrm{e} = W_\mathrm{e}$ holds and both strain energy density functions are equivalent. For pure transverse isotropy five material parameters and only the direction $\boldsymbol{v}_1$ of the fiber has to be defined. Further, the isotropic part can be replaced more easily by another isotropic strain energy density function as also shown in ref.[6].

Considering not only the elastic regime, the elastoplastic equations are based on the multiplicative split of the deformation gradient $\boldsymbol{F} = \boldsymbol{F}_\mathrm{e}\boldsymbol{F}_\mathrm{p}$ and are anisotropic with respect to their yield criterion. Based on the stress

$$\boldsymbol{\Xi} = 2\rho_0 \boldsymbol{C}\boldsymbol{F}_\mathrm{p}^{-1} \frac{\partial \Psi_\mathrm{e}}{\partial \boldsymbol{C}_\mathrm{e}} \boldsymbol{F}_\mathrm{p}^{-\mathrm{T}}, \tag{10}$$

the stress invariants are defined as

$$I_i = \mathrm{tr}[\boldsymbol{M}_i \mathrm{dev}\boldsymbol{\Xi}], \quad \text{for } i = 1, 2, 3, \tag{11}$$

$$I_{i+3} = \mathrm{tr}[\boldsymbol{M}_i (\mathrm{dev}\boldsymbol{\Xi})^2], \quad \text{for } i = 1, 2, 3. \tag{12}$$

TABLE 2 Elasto-plastic material parameters.

$\beta_1 = \frac{1}{{}^0\sigma_{11}^2} - \beta_7$	$\beta_4 = -(\frac{1}{{}^0\sigma_{11}^2} + \frac{1}{{}^0\sigma_{22}^2} - \frac{1}{{}^0\sigma_{33}^2})$	$\beta_7 = \frac{1}{2}(\frac{1}{{}^0\sigma_{12}^2} + \frac{1}{{}^0\sigma_{13}^2} - \frac{1}{{}^0\sigma_{23}^2})$
$\beta_2 = \frac{1}{{}^0\sigma_{22}^2} - \beta_8$	$\beta_5 = -(\frac{1}{{}^0\sigma_{11}^2} - \frac{1}{{}^0\sigma_{22}^2} + \frac{1}{{}^0\sigma_{33}^2})$	$\beta_8 = \frac{1}{2}(\frac{1}{{}^0\sigma_{12}^2} - \frac{1}{{}^0\sigma_{13}^2} + \frac{1}{{}^0\sigma_{23}^2})$
$\beta_3 = \frac{1}{{}^0\sigma_{33}^2} - \beta_9$	$\beta_6 = -(-\frac{1}{{}^0\sigma_{11}^2} + \frac{1}{{}^0\sigma_{22}^2} + \frac{1}{{}^0\sigma_{33}^2})$	$\beta_9 = \frac{1}{2}(-\frac{1}{{}^0\sigma_{12}^2} + \frac{1}{{}^0\sigma_{13}^2} + \frac{1}{{}^0\sigma_{23}^2})$

The stress invariants are then used to compute an equivalent stress

$$\chi = \sum_{i=1}^{3} \left[\beta_i I_i^2 + \beta_{i+6} I_{i+3} + \frac{1}{2} \sum_{j=1}^{3} \beta_{i+j+1} I_i I_j \right], \quad \text{for} i \neq j, \tag{13}$$

that is used to determine the yield criterion

$$\Phi = \sqrt{\frac{2}{3}} \left({}^0\sigma_{11} \sqrt{\chi} - ({}^0\sigma_{11} - Y) \right). \tag{14}$$

Herein, the material parameters $\beta_i, i = 1, .., 9$ are based on the yield stresses ${}^0\sigma_{ij}$, see Table 2. Assuming transverse isotropy as well for the yield surfaces the following equations hold: ${}^0\sigma_{12} = {}^0\sigma_{13}$, ${}^0\sigma_{22} = {}^0\sigma_{33}$, ${}^0\sigma_{23} = \frac{{}^0\sigma_{22}}{\sqrt{3}}$.

The nonlinear but isotropic hardening law is described as follows

$$Y(Z) = -HZ - (\sigma_\infty - {}^0\sigma_{11})(1 - e^{-\eta Z}), \tag{15}$$

where σ_∞ represents a saturation stress, H the linear hardening and η is the exponential hardening parameter, controlling the rate of the exponential hardening. A more detailed description of the model is presented in refs. [1, 3, 5, 7].

2.1 | *hp*-adaptivity

The main advantages of high-order finite elements are the accurate description of curved geometries and a higher accuracy compared to pure *h*-refinement. One major error contributor in high-order elements can be related to discontinuities, that are present within an element and thus cannot be represented by continuous shape functions. The interface between the elastic and the elastoplastic material (further called the plastic front) is an example, where an internal discontinuity is present, that usually does not adhere to element boundaries. This yields in a reduced accuracy within a cut high-order element.

There are different methods to overcome this problem, as re-meshing, *rp*-refinement [8] or *hp*-refinement [9], which are all based on the idea to resolve the plastic front through an element edge or face. All of the above methods require, that the history data related to the plastic strains has to be transferred. During a change of the discretization the integration points usually have to be redistributed and an interpolation of the history data to the new integration points is necessary.

A schematic workflow for nonlinear finite elements is shown in Figure 1. At the end of each load step (Figure 2A), the plastic front is detected by inspecting the properties of the integration points. After the positions have been determined the *hp*-refinement refines the mesh in a *h*- or *hp*-manner towards the plastic front to better resolve the arising discontinuity (Figure 2B). Depending on the number of subdivisions and the desired accuracy a graded mesh with reduced ansatz order can be chosen, to increase the efficiency of the overall computation. With the refined mesh the values of the new degrees of freedom are determined using a L_2-projection. Additionally new integration points are introduced and the history values are interpolated (Figure 2C). Finally the load step is repeated with the new discretization.

This process can be repeated several times but it is usually desired to be done only once or twice to prevent exhaustive additional computational resources. Refining towards the integration points on both sides of the plastic front, meaning adjacent elastic and elastoplastic integration points (marked in green in Figure 2B), increases the number of refined elements but reduces the probability of a second loop repeating the same load step once more.

As soon as a set of refined elements is completely plastified, hence they are not intersected by the plastic front, the elements will be coarsened up to their initial size. The workflow guarantees, that for the first refinement, there is no

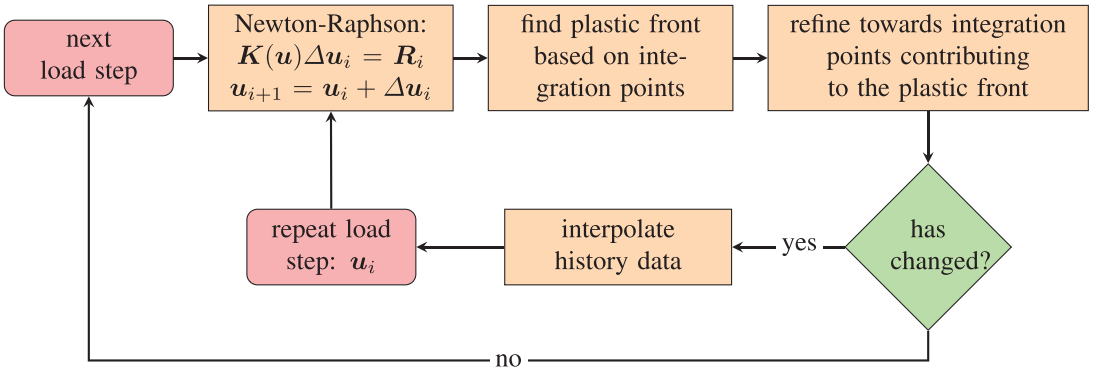

FIGURE 1 Schematic flow chart for the process of the adaptive refinement towards the plastic front.

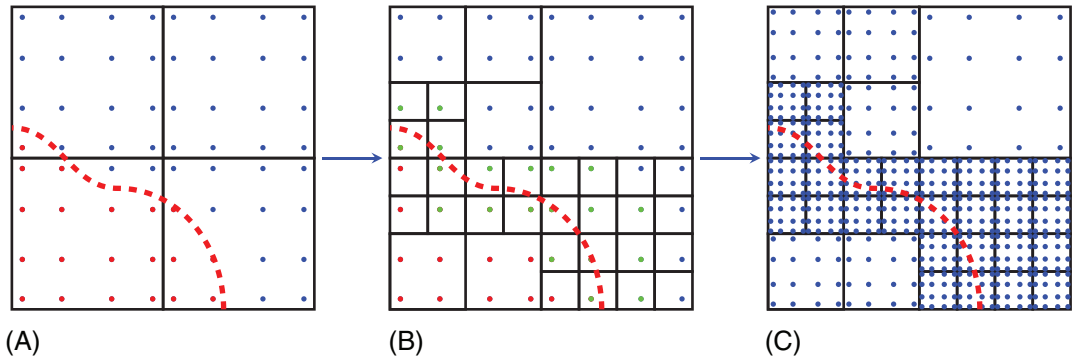

FIGURE 2 Schematic refinement procedure with a refinement depth of 2: (A) converged state with plastic front shown in red, (B) refined mesh with integration points involved in transition from elasticity to plasticity are marked in green, (C) refined mesh with new integration points.

history to be interpolated, as the refinement is conducted together with the progression of the plastic front. Thus, the interpolation of the history is only relevant for coarsening and for the refinement of already plastified elements. The latter one is important, when different loading directions are applied and multiple plastic fronts arise, or when the presented error estimation is combined with other error estimators.

Within this publication only bi-linear and tri-linear interpolation based on ref. [9] is considered. The interpolation is conducted within the local coordinate system of the element.

3 | RESULTS

To test the refinement algorithm the perforated plate example based on Stein et al. [10] is analyzed. The boundary conditions and simulation parameters can be found in Figure 4. For this purpose the simulation parameters are chosen to be $q_1 = 450$ MPa, $L = 100$ mm, $R = 10$ mm and the material parameters for finite J_2-plasticity are $E = 206.9$ GPa, $\nu = 0.29$, $\sigma_y = 450$ MPa, $\sigma_{inf} = 750$ MPa, $H = 129$ MPa, $\eta = 16.93$.

In Figure 4 the results of the perforated plate simulation for all five load steps from left to the right are shown. The adaptive refinement starts from the bottom corner at the inner circle and spreads together with the plastic front towards the upper left corner. In the first four load steps the mesh is only refined and no coarsening is present. With the fifth and last load step some of the elements within the plastic zone are also coarsened. In load step 4 and 5 are also some elements present, that are refined but do not exhibit the plastic front. This is a result of the broader range of refinement areas to prevent multiple re-computations of the same load step.

In Figure 5A comparison between different refinement strategies is shown for the final load step. For all simulations within the graph the trunk space [2] was used for the high-order shape functions. The black dashed line shows h-refinement using an ansatz order of $p = 2$, starting with 16 elements and increasing up to 10752 elements. In comparison

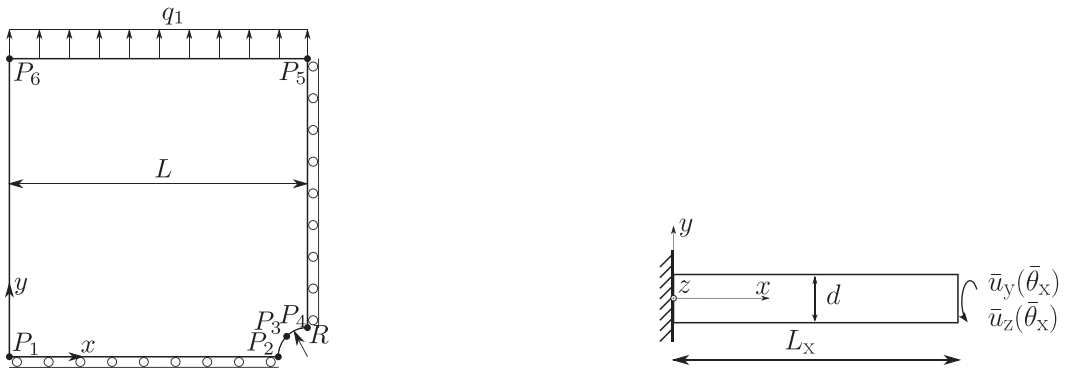

FIGURE 3 Simulation setup for the perforated plate (left) and the torsion test for a cable (right).

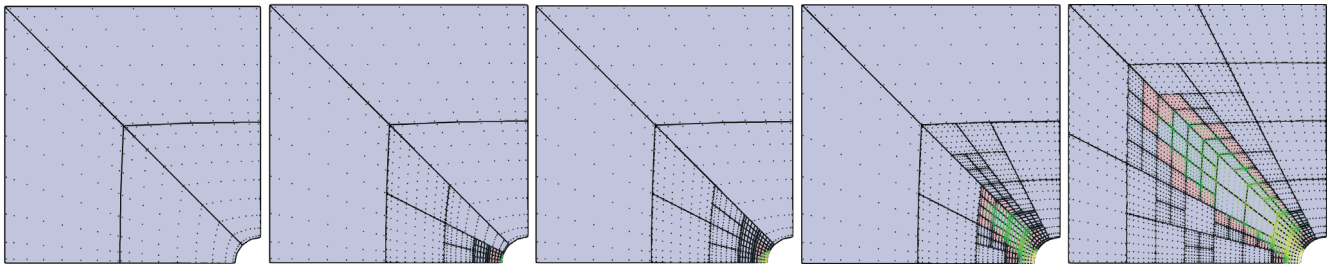

FIGURE 4 Simulation of the perforated plate in five load steps showing the equivalent plastic strain in green and the elements containing the plastic front in red.

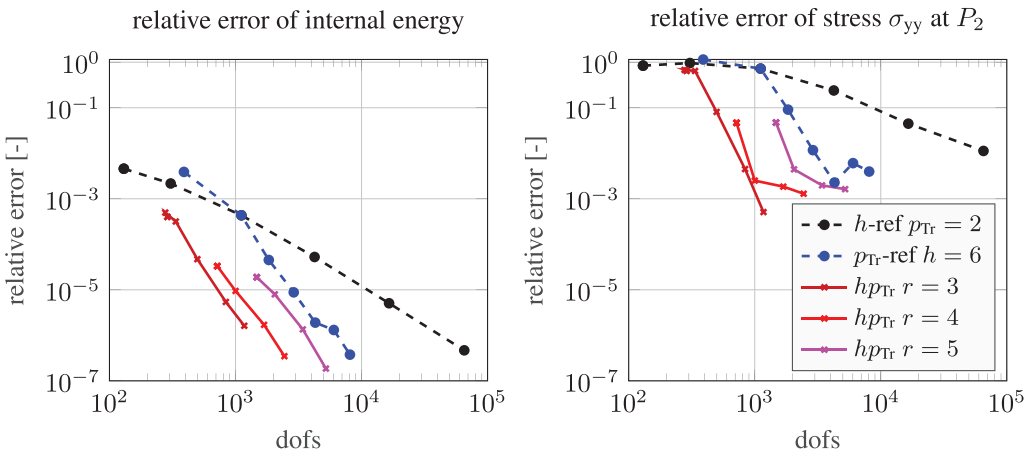

FIGURE 5 Convergence of the relative error of the strain energy and the stress σ_{yy} at point P_2 for the final load step.

the p-refinement is plotted as the blue dashed line having a constant number of 84 elements with increasing order p. Finally the dark red, red, and magenta line represent hp-refinement with four elements at the beginning as shown in Figure 4. The curve represents an increasing ansatz order p of the base mesh and the different colors correspond to the refinement depth $r = 3, 4, 5$ respectively. In addition to the adaptive h-refinement, the ansatz order is reduced by up to two orders $(p - 2)$ but always has a minimum of order $p = 2$ at the finest level (except if the base mesh is of order $p = 1$).

In Figure 5 the hp-refinement is located on the lower left side of the h-refinement and p-refinement, which indicates better convergence for the hp-refinement. The result for the stress σ_{yy} at point P_2 (see Figure 3) is similar, with the remark, that there is a drop of convergence visible for $r = 4, 5$. This drop of convergence is related to a coarsening at the corner of point P_2, that reduces to a refinement depth of $r = 3$ at this corner due to fully plastified elements. This drop of convergence can be overcome by applying additional error indicators, that capture these error sources as well. As a final remark, the

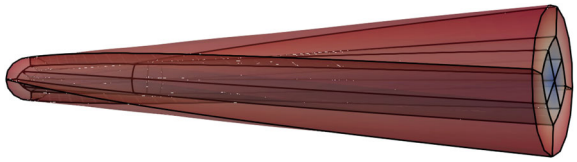

FIGURE 6 Simulation of the cable under torsion using the *hp*-refinement and only a single element along the axis.

computation of the number of degrees of freedom for *hp*-refinement is not straight forward, as the number of degrees of freedoms changes throughout the computation. For the convergence plots the number of degrees of freedom was averaged over the load steps as the previous load steps are relevant for the final results and influence the overall computational cost. This decreases the number of degrees of freedom in the convergence plot in comparison to the number of degrees of freedom used in the final load step, as can be deducted from the number of elements visible in Figure 4.

However, this demonstrates, that the *hp*-refinement is a valid option to adaptively resolve and capture the plastic front to a certain extent and overcomes the reduced convergence properties for higher order shape functions in elastoplastic simulations.

To demonstrate, that the method is also working in three dimensions, the torsion test shown in Figure 3 on the right-hand side is also conducted using the *hp*-refinement. Therefore, the material parameters $E_1 = 1000$ MPa, $E_2 = 600$ MPa, $G_{12} = 194.2$ MPa, $\nu_{12} = \nu_{22} = 0.4$, ${}^0\sigma_{11} = {}^0\sigma_{22} = 0.784$ MPa, ${}^0\sigma_{12} = 1.0$ MPa, ${}^0\sigma_{\text{inf}} = 1.5$ MPa, $H = 65.31$ MPa, and $\eta = 893.6$ based on ref. [7] are used for the material model presented in Section 2. The cable has a length of $L_x = 90.54$ mm, a diameter $d = 8.45$ mm and a maximum torsional displacement of 80° is applied.

In Figure 6 the final displacement of the cable is shown. A very coarse base mesh of five elements in the cross section and 1 element in axial direction was used with an ansatz order of $p = 4$ and a maximum refinement depth of $r = 1$, that refines towards the plastic front. Figure 6 shows, that the mesh is refined at the center and the inner element is split into eight sub-elements. This reflects the pure torsion that is applied, as the stress has its peak at the outer radius and reduces down to zero at the center. This leads to a plastic front that starts from the outside and progresses towards the center, while - in theory - never reaching it. This last example is only a demonstration of the application of *hp*-refinement to a three-dimensional cable. The goal is to use this method in combination with local contact of the cables and is subject to ongoing research.

4 | CONCLUSION

In this article the application of *hp*-refinement to elastoplastic problems was presented showing the general workflow and basic idea. The method was then applied to two elastoplastic problems, the perforated plate and a simulation of an elastoplastic cable subjected to torsion. While the simulated torsion test of the cable is mainly a demonstration, that the method is also applicable to three-dimensional problems and reflects the physical expectation of the progression of the plastic front, the perforated plate compares the convergence properties with standard high-order refinement methods. With the remark of how to measure the number of degrees of freedom for an adaptive mesh, the convergence graphs show, that the solution converges fast and in average uses a lower number of degrees of freedom to achieve similar accuracy as compared to pure *h*-refinement or pure *p*-refinement.

To this end this is a promising result, that requires further research with respect to the data transfer of the plastic history variables, that have to be transferred between the changing integration points during the adaptive refinement. In this work only the bi-/tri-linear interpolation has been used, which also showed good results for the presented problem.

ACKNOWLEDGMENTS

Open access funding enabled and organized by Projekt DEAL.

ORCID

André Hildebrandt-Raj https://orcid.org/0000-0001-9557-4549
Prateek Sharma https://orcid.org/0000-0001-6634-7881
Alexander Düster https://orcid.org/0000-0002-2162-3675

REFERENCES

1. Sansour, C., Karšaj, I., & Sorić, J. (2006). A formulation of anisotropic continuum elastoplasticity at finite strains. Part I: modelling. *International Journal of Plasticity*, *22*(12), 2346–2365.
2. Düster, A., Bröker, H., & Rank, E. (2001). The p-version of the finite element method for three-dimensional curved thin walled structures. *International Journal for Numerical Methods in Engineering*, *52*(7), 673–703.
3. Hildebrandt, A., & Düster, A. (2022). Numerical investigation of high-order solid finite elements for anisotropic finite strain problems. *International Journal of Computational Methods*, *19*(5), 2250007.
4. Zander, N., Bog, T., Kollmannsberger, S., Schillinger, D., & Rank, E. (2015). Multi-level hp-adaptivity: High-order mesh adaptivity without the difficulties of constraining hanging nodes. *Computational Mechanics*, *55*(3), 499–517.
5. Sansour, C., Karšaj, I., & Sorić, J. (2008). On a numerical implementation of a formulation of anisotropic continuum elastoplasticity at finite strains. *Journal of Computational Physics*, *227*(16), 7643–7663.
6. Bonet, J., & Burton, A. J. (1998). A simple orthotropic, transversely isotropic hyperelastic constitutive equation for large strain computations. *Computer Methods in Applied Mechanics and Engineering*, *162*(1-4), 151–164.
7. Hildebrandt, A., Prateek, S., Düster, A., & Diebels, S. (2022). Efficient simulation of cables with anisotropic high-order solid finite elements. *Mathematics and Mechanics of Solids*, *27*(10), 2314–2337.
8. Nübel, V., Düster, A., & Rank, E. (2007). An rp-adaptive finite element method for the deformation theory of plasticity. *Computational Mechanics*, *39*, 557–574.
9. Özcan, A., Kollmannsberger, S., Jomo, J., & Rank, E. (2019). Residual stresses in metal deposition modeling: Discretizations of higher order. *Computers & Mathematics with Applications*, *78*(7), 2247–2266.
10. Stein, E. (Ed.). (2002). *Error-controlled adaptive finite elements in solid mechanics*. John Wiley & Sons.

How to cite this article: Hildebrandt-Raj, A., Sharma, P., Diebels, S., & Düster, A. (2023). Nonlinear cable computations using high-order solid elements with *hp*-adaptive refinement for anisotropic plasticity. *Proceedings in Applied Mathematics and Mechanics*, *23,* e202300123. https://doi.org/10.1002/pamm.202300123